ARTICLE

Check for updates

Non-orthogonal cavity modes near exceptional points in the far field

Jingnan Yang[1], Shushu Shi[2], Sai Yan[2], Rui Zhu[2], Xiaoming Zhao[3], Yi Qin[4], Bowen Fu[1], Xiqing Chen[1], Hancong Li[1], Zhanchun Zuo [2], Kuijuan Jin [2], Qihuang Gong [1] & Xiulai Xu [1,5 ✉]

Non-orthogonal eigenstates are a fundamental feature of non-Hermitian systems and are accompanied by the emergence of nontrivial features. However, the platforms to explore non-Hermitian mode couplings mainly measure near-field effects, and the far-field behaviours remain mostly unexplored. Here, we study how a microcavity with non-Hermitian mode coupling exhibits eigenstate non-orthogonality by investigating the spatial field and the far-field polarization of cavity modes. The non-Hermiticity arises from asymmetric back-scattering, which is controlled by integrating two scatterers of different size and location into a microdisk. We observe that the spatial field overlap of two modes increases abruptly to its maximum value, whilst different far-field elliptical polarizations of two modes coalesce when approaching an exceptional point. We demonstrate such features experimentally by measuring the far-field polarization from the fabricated microdisks. Our work reveals the non-orthogonality in the far-field degree of freedom, and the integrability of the microdisks paves a way to integrate more non-Hermitian optical properties into nanophotonic systems.

[1] State Key Laboratory for Mesoscopic Physics and Frontiers Science Center for Nano-optoelectronics, School of Physics, Peking University, 100871 Beijing, China. [2] Beijing National Laboratory for Condensed Matter Physics, Institute of Physics, Chinese Academy of Sciences, 100190 Beijing, China. [3] Department of Physics and Institute of Theoretical Physics, University of Science and Technology Beijing, 100083 Beijing, China. [4] Guangdong Provincial Key Laboratory of Quantum Metrology and Sensing & School of Physics and Astronomy, Sun Yat-Sen University (Zhuhai Campus), Zhuhai 519082, China. [5] Peking University Yangtze Delta Institute of Optoelectronics, Nantong 226010 Jiangsu, China. ✉email: xlxu@pku.edu.cn

Hermiticity in quantum mechanics guarantees orthogonality and completeness of eigenstates in a Hermitian system. In contrast, eigenstates of a non-Hermitian system are usually non-orthogonal. The eigenstate non-orthogonality is the fundamental and distinct feature to reveal the non-Hermiticity[1,2], and provides the basis for key non-Hermitian phenomena such as the exceptional point (EP). In other words, the eigenstates and eigenvalues simultaneously coalesce at peculiar spectral singularities[3–6]. EP enables many counter-intuitive phenomena including the chiral absorption[7,8] and the strongly modified spontaneous emission[9,10]. Therefore, degrees of freedom that exhibit the eigenstate non-orthogonality are highly desired for functions of non-Hermitian quantum devices[11], such as discriminating non-Hermitian quantum states[12] and exploring non-Hermitian topological physics[13,14].

Recently, optical systems have been attracting increasing interests in studying non-Hermitian physics[15–19], such as the whispering gallery mode (WGM) microcavities with asymmetric backscattering[11,20], parity-time (PT) or anti-PT symmetry[16,21]. Such microcavities provide a platform to investigate the non-orthogonal modes in different degrees of freedom, such as propagation direction[11,22], resonance frequency[23], intensity and beam dynamics[24,25]. Another degree of freedom, far-field polarization, is correlated to the symmetry and the orthogonality of near field[26–28] and plays key roles in nanophotonics, such as single-photon sources[29], lasers[30], nonlinear frequency conversion[31] and topological optics[32] and structured light[33]. However, the measurement of WGM microcavities with non-Hermitian mode coupling or PT symmetry mainly relies on the near-field fiber coupling[11,23]. As such, far-field polarization features of such WGM microcavities remain unexplored.

We use an ensemble of quantum dots as internal broad-band light sources to enable the far-field excitation[34], and use integrated internal scatterers to reduce the effects of disturbances from using external scatterers in the far-field collection. By integrating internal scatterers such as air cuts, bulges or holes, non-Hermitian mode coupling can be obtained in the WGM microcavities[35–38]. Furthermore, compared to traditional cavities with non-Hermitian mode coupling realized by external scatterers or gain/loss, the integrated internal scatterers enable small-size designs with small mode volumes and large-scale on-chip integration. These two features provide the basis for studying non-Hermitian cavity quantum electrodynamics (QED) and quantum optical devices[9,39–42].

Here we study the polarization of far-field photoluminescence (PL) spectra from cavity modes in microcavities with non-Hermitian mode coupling around an EP. The non-Hermiticity in mode coupling is realized by the asymmetric backscattering from two internal weak scatterers of different size and location, and the mode non-orthogonality is further controlled by the relative angle between the two scatterers. We reveal the angle dependence of the spatial field distribution and the far field polarization as non-Hermitian features of the system. Approaching an EP, we observe that the spatial field overlap of two modes increases abruptly, and the far-field polarizations of two modes are nearly identical, corresponding to coalescent eigenstates at an EP. These polarization features are further demonstrated by experimental measurements of fabricated microdisks. Since our microdisks with internal weak scatterers can be integrated on-chip, the non-orthogonality based near- and far-field features enable further applications to integrate the non-Hermitian optical properties into nanophotonic systems.

Results

Theoretical analysis

Left and right eigenstates, $|\psi_i^L\rangle$ and $|\psi_i^R\rangle$, correspond to Hamiltonians H and $H^\dagger$, respectively[43]. In contrast

to a Hermitian system, in a non-Hermitian system we have $H \neq H^\dagger$. Therefore, the non-Hermitian system follows the bi-orthogonality $\langle\psi_i^L|\psi_j^R\rangle = \delta_{i,j}$, which is very challenging to be directly experimentally obtained. However, the self-orthogonality terms $\langle\psi_i^R|\psi_j^R\rangle$ and $\langle\psi_i^L|\psi_j^L\rangle$, which follow $\delta_{i,j}$ for a Hermitian system, do not vanish for $i \neq j$ for a non-Hermitian system. This is the intrinsic difference between Hermitian and non-Hermitian systems. The non-orthogonality $\langle\psi_i^R|\psi_j^R\rangle$ supports non-trivial phenomena such as chirality[11] and topology[44], therefore, it is one focus of theoretical and experimental investigations on non-Hermitian systems.

Non-Hermitian optical systems with non-Hermitian mode coupling have been achieved by the asymmetric backscattering between clockwise (CW) and counter-clockwise (CCW) traveling-wave modes in a WGM microcavity. These modes are quasinormal modes since the optical microcavity is non-conservative with energy loss[45–47]. We only focus on well confined transverse electric (TE) modes in the first radial order with a high quality (Q) factors[48] and dominating E_x, E_y and H_z components, which can be easily experimentally observed in far-field photoluminescence (PL) spectra from microcavities with embedded self-assembled quantum dots as excitation sources[37,49–52]. Here the TE modes are labeled by $TE_{1,m}$ with the azimuthal mode number m. The cavity mode function follows $\psi_{CW} \propto e^{-im\phi}$ and $\psi_{CCW} \propto e^{im\phi}$ thus has $2m$ antinodes along the cavity perimeter. ϕ is the azimuthal angle in the polar coordinate.

WGMs are very sensitive to nano-scale perturbations[53–56]. These perturbations act as Rayleigh scatterers that introduce the backscattering coupling between CW and CCW modes, which are degenerate without scatterers. The non-Hermiticity in WGM mode coupling can be realized and modulated by the asymmetric backscattering from weak scatterers[20] or strong scatterers[38]. Here we consider a WGM cavity with two weak scatterers and use a two-mode approximation based Hamiltonian picture to analyze how the non-Hermiticity is controlled by the scatterers. The corresponding Hamiltonian using the traveling-wave basis $|\psi_{CW}^R\rangle$ and $|\psi_{CCW}^R\rangle$ is written as

$$H = \begin{pmatrix} \omega_0 + \omega' & A + Be^{-i2m\beta} \\ A + Be^{i2m\beta} & \omega_0 + \omega' \end{pmatrix}. \quad (1)$$

The terms A and B are complex because the scatterers induce a frequency shift and extra loss to the cavity modes, and they describe the backscattering effect from the two different weak scatterers, respectively. For more details about the two-mode approximation model, see Supplementary note 3 in supplementary materials (SMs). ω_0 is the complex eigenvalues for the unperturbed microcavity, ω' represents the complex frequency shift resulting from the two scatterers, and β is the relative angle between the two scatterers, as illustrated in Fig. 1a. Eigenvalues and eigenstates can be obtained respectively as

$$\omega_{1,2} = \omega_0 + \omega' \pm \sqrt{A^2 + B^2 + 2AB\cos(2m\beta)}, \quad (2)$$

$$\left|\psi_{1,2}^R\right\rangle = M\left|\psi_{CW}^R\right\rangle \pm N\left|\psi_{CCW}^R\right\rangle. \quad (3)$$

$M = \sqrt{A + Be^{-i2m\beta}}/\sqrt{2A + 2B\cos(2m\beta)}$ and $N = \sqrt{A + Be^{i2m\beta}}/\sqrt{2A + 2B\cos(2m\beta)}$. The eigenfrequencies are periodically modulated by β with period $P = 180°/m = 15°$ for $m = 12$. To quantify the eigenstate non-orthogonality, we introduce $\cos(\theta_{eigm}) = \langle\psi_1^R|\psi_2^R\rangle$, where we call $|\psi_1^R\rangle$ and $|\psi_2^R\rangle$ orthogonal (coalescent) if $\cos(\theta_{eigm}) = 0$ ($\cos(\theta_{eigm}) = 1$).

When the two weak scatterers differ ($A \neq B$), eigenstates exhibit non-orthogonality. In particular, EPs can be realized when one of the
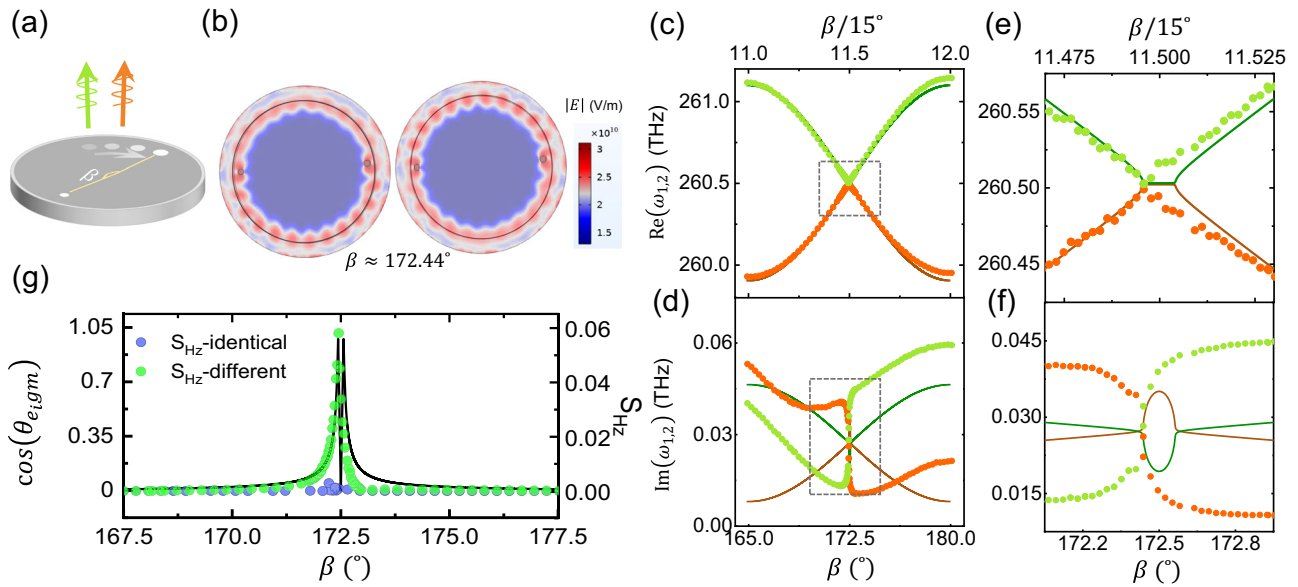
Fig. 1 Simulation and theoretical results for a microcavity with two scatterers. a Illustration of a microdisk integrated with two holes. **b** Simulated near-field $|E|$ distribution of two modes close to an EP with $\beta \approx 172.44°$. Here $r_1 = 0.037285\,\mu m$, $r_2 = 0.03203\,\mu m$, $d_1 = 0.73312\,\mu m$, $d_2 = 0.74995\,\mu m$. Theoretical (solid lines) and simulated (dots) complex frequencies of two modes respectively colored in green and orange with their real parts (**c**) and imaginary parts (**d**). **e, f** Magnified regions labeled by dashed squares in **c** and **d**. **g** $\cos(\theta_{eigm})$ (solid black line) and S_{H_z} varying with β for two different holes (green dots) and two identical holes (blue dots).

non-diagonal terms of H in Eq. (1) vanishes near $\beta = (L + 1/2) \times 15°$ (L is an integer) and H becomes defective[20,57]. To further explore the non-Hermiticity, we calculate the dependence of $\omega_{1,2}$ and $\cos(\theta_{eigm})$ on β for $m = 12$, and present the results in Fig. 1c–g. The values for A, B and $\omega_0 + \omega'$ are deduced from complex eigenfrequencies in simulation results, for details see *Theoretical calculations of eigenvalues* in Methods. From eigenvalues in Eq. (2), it can be inferred that non-Hermitian degeneracy happens when $A^2 + B^2 + 2AB \cos(2m\beta) = 0$, which is possible when $|A| \approx |B|$, $\cos(2m\beta) \approx -1$ and $\sin(2m\beta) \approx 0$. For every $\beta = (L + 1/2) \times 15°$, there are two different β that can satisfy this requirement, but correspond to different eigenmodes. As shown in Fig. 1e, f, resonance frequencies (e) and decay rates (f) of two modes become degenerate symmetrically around $\beta = 172.5°$ with two EPs.

Simulation results. We implement numerical simulations using the finite element method. To control the non-Hermiticity, cylinder air holes are set in the microdisks with a thickness of 250 nm and a radius of 1 μm as shown in Fig. 1a. The two scatterers are defined by the radius $r_{1,2}$, the distance from the microdisk center $d_{1,2}$ and the relative angle β. We use $r_{1,2} = 37.285, 32.03$ nm and $d_{1,2} = 733.12, 749.95$ nm, which follows $r_1 > r_2$ and $d_1 < d_2$ to achieve $|A| \approx |B|$ for an EP[20]. Details about the designs and the simulation methods are presented in Methods and Supplementary note 1 in SMs.

We focus on the spatial field distribution and far-field polarization of the two modes. At an EP, two modes propagate as traveling waves and coalesce into one mode with the same complex eigenfrequencies. As shown in Fig. 1b, the contrast between near-field antinodes and nodes for $\beta \approx 172.44°$ becomes vague, exhibiting features similar to traveling waves. More obvious features like traveling waves rather than standing waves can be seen in Supplementary Fig. S1(j) in SMs. Meanwhile, two modes have almost the same complex eigenvalues as shown in Fig. 1e, f. E_x and E_y components of two modes distributed along a black circle on the microdisk surface as shown in Fig. 1b highly

coincide at $\beta \approx 172.44°$ as shown in Fig. 2a. In contrast, when away from the EP (e.g., $\beta \approx 165°$), an obvious spatial phase difference exists between E_x and E_y components of the two modes, as shown in Fig. 2a. To describe the spatial field overlap of two modes, we define S_k ($k = E_x, E_y$ or H_z) to quantify the non-orthogonality. Take H_z for example, we have

$$S_{H_z} = \left| \int H_{z1}{}^* H_{z2} dV \right|, \qquad (4)$$

where H_{zi} is the normalized field extracted from the simulations. The normalization considers the field in the perfectly matched layer due to the non-Hermiticity of the quasinormal modes[45]. For details of the normalization, see *Normalization of simulated spatial field* in Methods. Figure 1g shows $\cos(\theta_{eigm})$ from the two-mode picture Eq. (1) and S_{H_z} for two different holes (labeled by green circles) from the simulation with varying β. Both two parameters, which quantify the non-orthogonality, increase abruptly when approaching the EP and reach their maximum values at the EP. Similar changes also apply to S_{E_x} (blue crosses) and S_{E_y} (purple dots) as shown in Fig. 2a, which exhibit the same trend but in a larger ratio versus β compared to S_{H_z}. By comparison, such high non-orthogonality is not observed for two identical holes as shown by the results in Fig. 1(g) (labeled by blue circles) and Supplementary Fig. S2(c) and (d) in Supplementary note 2 in SMs. The near-field distributions are strongly molded by the holes because of their direct effects on the eigenstate non-orthogonality. By comparison, the extra energy loss of the cavity caused by the scatterers is relatively weakly molded because it is affected by the spatial overlap between scatterers and mode field.

Note that $\cos(\theta_{eigm})$ in Fig. 1g indicates two EPs while S_{H_z} only responds to one EP at $\beta \approx 172.44°$. Another EP is expected to appear at $\beta \approx 172.56°$ based on the two-mode picture (Eq. (1)). The deviation lies in the imperfection of the two-mode approximation model we use instead of the imperfection of the simulation mesh size, for example, only considering TE modes
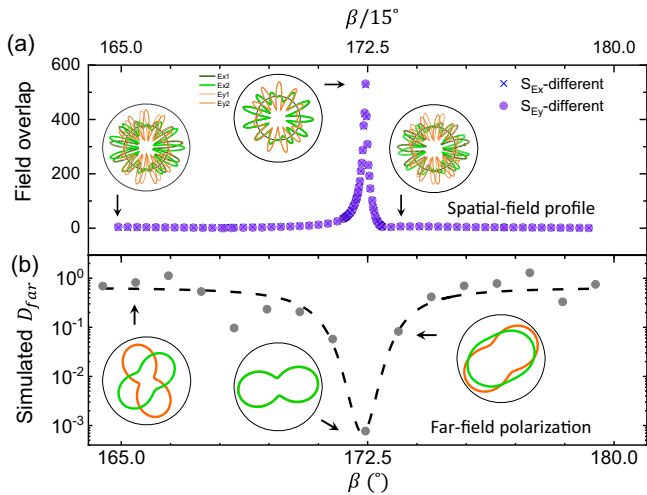
Fig. 2 Simulation results for the spatial field overlap and the far-field polarization. a S_{E_x} (blue crosses) and S_{E_y} (purple dots) of two modes for two different scatterers where the maximum value corresponds to high coalescence while the minimum values correspond to high orthogonality. Insets: E_x (green lines) and E_y (orange lines) of two modes (subscript 1 and 2) with distributed along a black circle inside the microdisks for three different β as shown in Fig. 1b. **b** Far field polarization difference D_{far} between two modes labeled by gray dots. The dashed gray line is the Lorentz fitting curve. Insets: polar maps of normalized polarization ellipses of two modes colored in orange and green for different β by setting the ellipse area as 1.

with a fixed m is not a good assumption for internal scatterers[36] and A and B in the Hamiltonian H are not always constant for different β. Indeed, the two EPs correspond to two slightly different sets of scatter designs as predicted by the local basis theory[58], rather than the same design predicted by the two-mode picture using global basis. Further development is still needed to improve for theoretically describing such WGM cavities with non-Hermitian scattering physical process with multiple weak scatterers, especially near EPs. Nevertheless, our conclusions are further verified with the numerical simulations by solving Maxwell's equations considering the propagation laws in different media and materials and subsequent experimental demonstrations.

The far-field polarization is correlated to the symmetry of the near-field distribution inside a cavity. For the cavity mode with highly symmetric near-field distribution, such as the L3 photonic crystal cavity, the linear far-field polarization can be predicted according to the parities of their in-plane electric field components[26,27]. However, asymmetric backscattering redistributes the near field and disturbs the symmetry of mode field distribution, which makes the polarization very complex. In contrast to the linear polarization in an L3 cavity, elliptical polarizations with different polarization angles and polarization degrees are obtained for the two modes in the WGM cavities with non-Hermitian mode coupling. The numerical simulation results of typical cases are presented in the insets in Fig. 2b. To describe the difference between two polarization ellipses, we consider both polarization angle and polarization degree and define

$$D_{far} = \frac{|P_1 - P_2|}{P_1 + P_2} + \frac{P_1 + P_2}{2}\sin(\Delta\gamma). \quad (5)$$

P_1 and P_2 are the polarization degrees of two modes, defined as the ratio of the major axis a to the minor axis b in the polarization

ellipse, while $\Delta\gamma$ is the polarization angle difference (0° to 90°) between two modes, which are illustrated in Supplementary Fig. S4a in supplementary materials. The first term of D_{far} describes the difference originating from the polarization degree difference between two modes, while the second term describes the difference originating from the polarization angle difference between two modes. For the second term, we multiply the polarization angle difference $\sin(\Delta\gamma)$ by the averaged polarization degree $(P_1 + P_2)/2$. This is because when approaching the circular polarization ($P_{1,2} \approx 0$), the difference in the polarization angle has less physical meaning. As shown in Fig. 2b, D_{far} decreases when approaching an EP and reaches the minimum value at an EP. The polar maps of two polarization ellipses can vary from relatively large $\Delta\gamma$ with $P_1 \neq P_2$ to relatively small $\Delta\gamma$ also with $P_1 \neq P_2$, and coalesce as $\Delta\gamma = 0$ and $P_1 = P_2$ at the EP.

Experimental results. To experimentally demonstrate the far-field features, we fabricated microcavities with two holes according to the simulation results. We span β from 160° to 200° with 1° increment, and fabricate five identical microdisks for each parameter. Figure 3a shows the typical SEM images, recorded for two microdisks with different β. We use InAs quantum dots embedded inside the microdisks as the broad-band light sources for the far-field excitation of the cavity modes. In principle, all the cavity modes in the spectral range of PL emission from the ensemble of quantum dots (QDs) can be observed and be tuned for achieving EPs if with proper scatterer design. However, we only focus on $TE_{1,12}$ mode in this work. Specific details on the fabrication method and experimental setup can be found in Methods.

Figure 3b shows the PL spectra recorded from the microdisks with different β. As shown, we observe that a pair of split peaks gradually emerge into one peak at $\beta = 173°$ and $\beta = 187°$, in agreement with the $\beta \approx 11.5 \times 15°$ and $\beta \approx 12.5 \times 15°$ for realizing EPs predicted in theory discussed above. Figure 3c, d show the statistics of the fitting results of the frequency splitting (c) and the decay rates (d) of the two modes. Here in Fig. 3c we use the difference between two mode frequencies, because the absolute cavity resonance wavelengths contain fluctuations arising from random fabrication errors and intrinsic backscattering[54].

In Fig. 4a we present the experimental results of far-field polarization extracted from the PL spectra. As shown, D_{far} varies quasi-periodically with β with two clear dips in Fig. 4a, corresponding to the coalescent polar maps of polarization ellipses predicted approaching an EP (Fig. 2b). The polarizations in three typical cases are presented in Fig. 4b–d, corresponding to the three pink dots in Fig. 4a. The case of $\beta = 165° = 11 \times 15°$ in Fig. 4b corresponds to a small spatial overlap (165° in Fig. 2a) with the maximum frequency splitting and decay rate difference. As expected, the experimental polarization of spectra (Fig. 4b) shows that the polarization angle difference can reach up to $\Delta\gamma = \pi/2$, in good agreement with the prediction in Fig. 2b. In contrast, for $\beta = 173° \approx 11.5 \times 15°$ in Fig. 4c, polar maps of two polarization ellipses have almost the same polarization angles but different polarization degrees. For $\beta = 187° \approx 12.5 \times 15°$ in Fig. 4d, polar maps of two polarization ellipses are almost identical. These cases are consistent with the corresponding cases approaching EP as predicted in Fig. 2b. The good agreement between the theory and the experiment further strengthens our conclusion that the far-field polarization is modulated by the eigenstate non-orthogonality in an optical microcavity with non-Hermitian mode coupling.

Discussion

Due to the small scale of holes, fabricated active microdisks with two holes can still allow both small mode volume and high quality
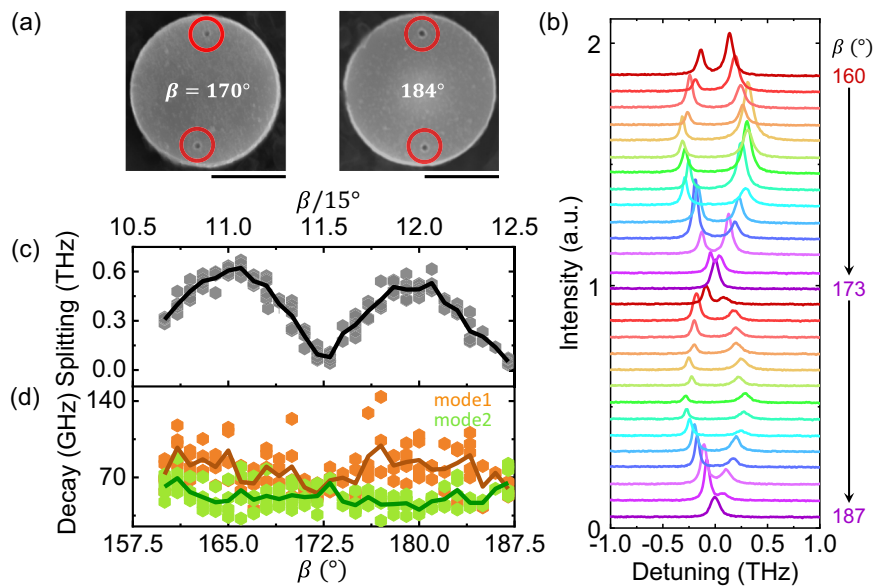
Fig. 3 Experimental far-field PL spectra from fabricated microcavities with different β. a Scanning electron microscope (SEM) images of fabricated microdisks with two holes labeled by red circles for $\beta = 170°$ and $\beta = 184°$. The scale bars are 1 μm. **b** PL spectra of cavity modes for β from 160° to 187°. Here the center resonance frequency of each doublet is set as 0 THz for a better demonstration. Statistics of fitting results of resonance frequency splitting (**c**) and decay rates (**d**) of two modes.

factors as shown in Supplementary Fig. S3c, d. As they are non-Hermitian systems with controllable near-field distribution and far-field polarization, such microcavities show great application potential in polarization-controllable low-threshold lasers or single-photon sources, and in the study of non-linear optics and cavity QED. Furthermore, using internal degrees of freedom of light, such as frequency and orbital angular momentum, researchers have proposed to use coupling between different modes to configure synthetic dimensions[59], which can be used for simulating one-dimensional or two-dimensional non-Hermitian topological systems[60–63]. For the cavity in this work, due to the effects of holes on all the modes, m in Eq. (1) can represent any different mode. Therefore, by introducing a coupling between different modes, extra synthetic dimensions could be configured for simulating non-Hermitian topological systems to study rich physical phenomena, such as PT phase transition, non-Hermitian skin effect and novel topological states. The far field polarization can provide observable channels for understanding the intrinsic topological physics of these phenomena[32,63].

In summary, we integrate two different scatterers into active microdisks and obtain controllable non-Hermitian systems with non-orthogonal eigenstates. The eigenstate non-orthogonality is revealed by the spatial field overlap and the far field polarization of cavity modes through numerical simulations where high non-orthogonality corresponds to a large spatial-field overlap and a small difference in polarization angle and polarization degree. Further experimental measurements of far-field polarization of the PL spectra of cavity modes demonstrate such far-field polarization features predicted in simulations. Experimental demonstration of controllable non-Hermitian systems can inspire more integrated optical devices based on controllable non-orthogonal eigenstates. Meanwhile, such microcavities with non-Hermitian mode coupling have potential applications in simulating high-dimensional non-Hermitian topological systems using extra synthetic dimensions to study novel physical phenomena.

Methods

Theoretical calculations of eigenvalues. To analyze how the scatterers affect the microdisks, we calculate the eigenvalues and eigenstates for the two different scatterers. We directly set values to A and B, which actually considers the mutual effects on backscattering from each another. A and B are obtained by calculating the eigenvalues at $\beta = 165°$ and $\beta \approx 172.44°$ close to an EP. For $\beta = 165°$, we have $\delta(\omega) = 2\sqrt{A^2 + B^2}$. For $\beta_{EP} \approx 172.44°$ near an EP, we have $\delta(\omega) = 2\sqrt{A^2 + B^2 + 2AB\cos(2m\beta_{EP})}$. By calculating these two equations, we can deduce the complex values of A and B. Here $A = 0.2985 + 0.0135i$, $B = 0.2990 + 0.0056i$. While if we use eigenvalues for $\beta_{EP} \approx 172.44°$ and $\beta \approx 187.19°$, we have $A = 0.0231 + 0.0089i$ and $B = 0.0234 + 0.0077i$. Obviously, two sets of A and B are different. For the two different scatterers, $r_1 = 0.037285$ μm, $r_2 = 0.03203$ μm, $d_1 = 0.73312$ μm, $d_2 = 0.74995$ μm.

Simulation method for spatial field. To numerically compute the complex eigenfrequencies and spatial field of $TE_{1,12}$ quasi-normal modes in a microdisk, we use a simulation method based on the finite element method to study the wave optics in a whispering galley mode (WGM) microcavity. The model we simulate contains a microdisk with two holes, an outer air layer (a column with radius of 2.2 μm and height of 2.65 μm removing the microdisk in the center) and a perfectly matched layer (PML) (a column with radius of 2.8 μm and height of 4.0 μm removing the microdisk and air layer) which absorbs the waves emitting outwards in different directions and in different wavelength in spectra from the microdisk. The refractive index of GaAs for simulation is $n = 3.44$. Complex eigenfrequencies (ω) of modes can be directly obtained, of which real and imaginary parts represent the resonance frequency and the energy loss rate, respectively. The imaginary parts mainly result from the radiation loss due to the curved edge of the microdisk as well as the
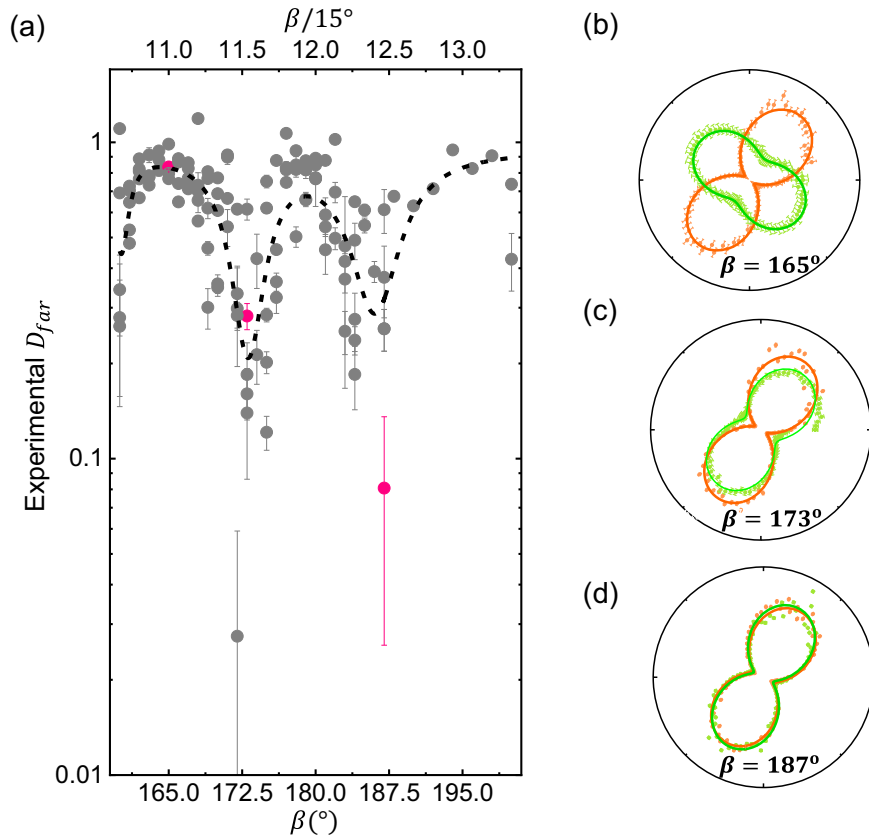
Fig. 4 Experimental far-field polarization results from fabricated microcavities with different β. a Experimental D_{far} labeled by gray and pink dots between two polarization ellipses of two modes varying with β. The dashed line is a fitting curve. **b–d** Polar maps of two normalized polarization ellipses for $\beta = 165°$, $\beta = 173°$ and $\beta = 187°$ corresponding to the pink dots in **a**. The green and orange dots refer to the experimental PL intensity fitting data with error bars when rotating the $1/2\lambda$ waveplate and the solid lines refer to theoretical fits. The relative larger error bars in **b** are due to the weaker PL intensities in experiments.

scattering loss from scatterers. The Q factor is calculated by $Q = \frac{Re(\omega)}{2Im(\omega)}$.

Normalization of simulated spatial field. To calculate the overlap of the spatial field of two quasinormal modes, we need to post-process the simulation results to obtain the integral of two normalized field components from two different quasinormal modes. The mode field we obtain from the simulation are initially not normalized. For the normalization of simulation results, we follow the quantized cavity mode field, which is

$$E(r) = i\sqrt{\frac{\hbar\omega}{2\varepsilon_r\varepsilon_0}}(a\alpha(r) - a^+\alpha^*(r)). \quad (6)$$

ω is the cavity mode frequency. ε_0 (ε_r) is the vacuum (relative) permittivity. a/a^+ is the ladder operator of photons. $\alpha(r)$ is the normalized cavity mode function which means $\int\alpha(r)\alpha^*(r)dV = 1$. Therefore, based on the simulated electric field E_{cal}, we normalize and get the cavity mode function as

$$\alpha(r) = \frac{n(r)E_{cal}(r)}{\sqrt{sum}}. \quad (7)$$

Here $sum = \int|n(r)E_{cal}(r)|^2dV$. Then we get the normalized electric field $E(r)$ by

$$E(r) = \sqrt{\frac{\hbar\omega}{2\varepsilon_r\varepsilon_0}}\alpha(r). \quad (8)$$

Finally we have

$$E(r) = \sqrt{\frac{\hbar\omega}{2\varepsilon_0 sum}}E_{cal}(r). \quad (9)$$

Here normalization coefficient is $c = \sqrt{\frac{\hbar\omega}{2\varepsilon_0 sum}}$.

After the normalization of the simulated field, the spatial field overlaps between field components of two quasinormal modes are calculated. Considering the non-Hermiticity of quasinormal modes, the volume integration to calculate $sum = \int|n(r)E_{cal}(r)|^2dV$ and spatial field overlap both consider PML, according to PML-based normalization in[45]. The refractive index $n(r)$ is set to different values according to the specific material with $n(r) = 1$ for air and PML while $n(r) = 3.44$ for GaAs. V includes all the simulation space including the air layer, the PML and the microdisk with two holes. Therefore, $|\int H_{z1}^*H_{z2}dV|$, $|\int E_{x1}^*E_{x2}dV|$ and $|\int E_{y1}^*E_{y2}dV|$ can be calculated as S_{H_z}, S_{E_x} and S_{E_y}, respectively.

Simulation method of far-field polarization. To calculate the far-field polarization ellipse, we use another method, the finite difference time domain method (FDTD). The simulation model is the same as above. Randomly positioned magnetic dipoles with random phases are set inside the microdisk cavity as excitation sources to simulate quantum dots embedded inside microdisks. Far-field polarization is exhibited through plotting a polarization

ellipse with the ellipse polarization angle and polarization degree based on the s and p polarization components with the zero-order diffraction $(0, 0)$ considered.

The sample. The sample we used for fabricating the microdisks was grown by molecular beam epitaxy. It is constituted from bottom to top by a GaAs substrate, an AlGaAs layer of 1 μm in thickness and a GaAs slab of 250 nm in thickness. One layer of InAs QDs is grown in the middle of the GaAs slab, which works as excitation sources with a spectral emission range from 250 to 333 THz.

The fabrication process. To obtain fabricated microdisks, a mask on the sample surface was first patterned with the designed structures by the electron beam lithography. Then the sample with the mask was etched by inductively coupled plasma to transfer the pattern on the mask onto the GaAs slab and the AlGaAs layer. Finally the sample with the mask removed was etched by HF solutions where most of AlGaAs under the microdisk is etched away. In the end, microdisk devices with an AlGaAs pedestal below were obtained.

Optical measurement. The optical measurement of fabricated microdisks was implemented with a conventional confocal micro-photoluminescence (PL). The microdisk devices were positioned in a sealed chamber cooled down to 10 K by the liquid helium flow. The QDs were first indirectly excited by a laser with an emission wavelength of 532 nm, and then the PL emission of the ensemble of QDs in a wide spectral range further excited the microdisk modes. The radiating PL spectra from microdisks were collected by a high-NA objective lens and then reflected and focused by a series of optical elements onto a linear array of InGaAs detectors dispersed through a spectrometer. The far-field polarization of the cavity modes was measured through putting a rotating $1/2\lambda$ waveplate and a polarizer in the light route and in front of the spectrometer. After traveling through a $1/2\lambda$ wave-plate, the polarization rotating angle of PL related to the polarizer, corresponds to twice the rotating angle $\alpha_{1/2\lambda}$ of the $1/2\lambda$ wave-plate, which is $2\alpha_{1/2\lambda}$.

Experimental polarization data analysis. The cavity modes exhibit elliptic polarization in the far-field. For a polarization ellipse, polarization degree P_i (polarizability) and polarization angle γ_i (major axis angle) are used to describe it. Here P_i is obtained by fitting the intensity curve of PL spectra of two modes. The data is obtained through multiple-peak Lorentz fitting the intensities of PL spectra of two modes when varying the rotating angle $\alpha_{1/2\lambda}$ of $1/2\lambda$ wave-plate, as shown in Supplementary Fig. S4a, b in Supplementary note 4. Then a sine function $y = y0 + |A|\sin(a(\gamma - \gamma_c))$ is used to fit the intensity curve with varying $2\alpha_{1/2\lambda}$. Finally, the polarization degree P_i is obtained by calculating $P_i = (|A| + y0)/(|A| - y0)$ and the polarization angle difference $\Delta\gamma$ is obtained by calculating $\Delta\gamma = \gamma_2 - \gamma_1$. The major axis is $a = (|A| + y0)/2$ and the minor axis $b = (|A| - y0)/2$. The polarization ellipse is normalized by normalizing the area $S = \pi(|A| + y0)/(|A| - y0)/4$ to 1 as shown in Fig. 4. Inversely, the polar maps of polarization ellipses in Fig. 2b can be obtained when the polarization degree and the polarization angle are known. To describe the difference between two polarization ellipses, we define a parameter by considering both the differences in major angle and polarization degree as

$$D_{far} = |(P_1 - P_2)/(P_1 + P_2)| + 0.5(P_1 + P_2)\sin(\Delta\gamma). \quad (10)$$

Here P_1 and P_2 are the polarization degrees of two quasinormal modes defined by the ratio of the long axis to the short axis in the

polarization ellipse. $|(P_1 - P_2)/(P_1 + P_2)|$ describes the difference in polarization degree for two quasinormal modes and $0.5(P_1 + P_2)\sin(\Delta\gamma)$ describes the difference in polarization angle multiplying the average polarization degree of two quasinormal modes. For example, for two identical polarization ellipses, $D_{far} = 0$. For two polarization ellipses with different polarization degrees and $\Delta\gamma = \pi/2$, $D_{far} = |(P_1 - P_2)/(P_1 + P_2)| + 0.5(P_1 + P_2)$.

Data availability
Relevant data supporting the key findings of this study are available within the article and the Supplementary Information file. All raw data generated during the current study are available from the corresponding authors upon request.

References
1. Ashida, Y., Gong, Z. & Ueda, M. Non-Hermitian physics. *Adv. Phys.* **69**, 249 (2020).
2. Rotter, I. A non-Hermitian hamilton operator and the physics of open quantum systems. *J. Phys. A Math. Theor.* **42**, 153001 (2009).
3. Gao, T. et al. Observation of non-Hermitian degeneracies in a chaotic exciton-polariton billiard. *Nature* **526**, 554 (2015).
4. Dembowski, C. et al. Encircling an exceptional point. *Phys. Rev. E* **69**, 056216 (2004).
5. Cartarius, H., Main, J. & Wunner, G. Exceptional points in atomic spectra. *Phys. Rev. Lett.* **99**, 173003 (2007).
6. Ding, K., Ma, G., Zhang, Z. Q. & Chan, C. T. Experimental demonstration of an anisotropic exceptional point. *Phys. Rev. Lett.* **121**, 085702 (2018).
7. Soleymani, S. et al. Chiral and degenerate perfect absorption on exceptional surfaces. *Nat. Commun.* **13**, 599 (2022).
8. Wang, C. et al. Electromagnetically induced transparency at a chiral exceptional point. *Nat. Phys.* **16**, 334 (2020).
9. Lu, Y., Zhao, Y., Li, R. & Liu, J. Anomalous spontaneous emission dynamics at chiral exceptional points. *Opt. Express* **30**, 41784 (2022).
10. Kim, J. et al. Practical lineshape of a laser operating near an exceptional point. *Sci. Rep.* **11**, 6164 (2021).
11. Peng, B. et al. Chiral modes and directional lasing at exceptional points. *Proc. Natl Acad. Sci. USA* **113**, 6845 (2016).
12. Chen, D.-X. et al. Quantum state discrimination in a $\mathcal{PT}$-symmetric system. *Phys. Rev. A* **106**, 022438 (2022).
13. idemann, S. et al. Topological funneling of light. *Science* **368**, 311 (2020).
14. Ding, K., Ma, G., Xiao, M., Zhang, Z. Q. & Chan, C. T. Emergence, coalescence, and topological properties of multiple exceptional points and their experimental realization. *Phys. Rev. X* **6**, 021007 (2016).
15. Miri, M.-A. & Alú, A. Exceptional points in optics and photonics. *Science* **363**, eaar7709 (2019).
16. Feng, L., El-Ganainy, R. & Ge, L. Non-Hermitian photonics based on parity–time symmetry. *Nat. Photonics* **11**, 752 (2017).
17. Hassan, A. U., Zhen, B., Soljačić, M., Khajavikhan, M. & Christodoulides, D. N. Dynamically encircling exceptional points : Exact evolution and polarization state conversion. *Phys. Rev. Lett.* **118**, 093002 (2017).
18. Hassani Gangaraj, S. A. & Monticone, F. Topological waveguiding near an exceptional point: Defect-immune, slow-light, and loss-immune propagation. *Phys. Rev. Lett.* **121**, 093901 (2018).
19. Li, Y., Liang, C., Wang, C., Lu, C. & Liu, Y.-C. Gain-loss-induced hybrid skin-topological effect. *Phys. Rev. Lett.* **128**, 223903 (2022).
20. Wiersig, J. Structure of whispering-gallery modes in optical microdisks perturbed by nanoparticles. *Phys. Rev. A* **84**, 063828 (2011).
21. Zhang, F., Feng, Y., Chen, X., Ge, L. & Wan, W. Synthetic anti-PT symmetry in a single microcavity. *Phys. Rev. Lett.* **124**, 053901 (2020).
22. Biasi, S., Franchi, R., Mione, F. & Pavesi, L. Interferometric method to estimate the eigenvalues of a non-hermitian two-level optical system. *Photon. Res.* **10**, 1134 (2022).
23. Chen, W., Kaya Özdemir, Ş., Zhao, G., Wiersig, J. & Yang, L. Exceptional points enhance sensing in an optical microcavity. *Nature* **548**, 192 (2017).
24. Makris, K. G., El-Ganainy, R., Christodoulides, D. N. & Musslimani, Z. H. Beam dynamics in $\mathcal{PT}$ symmetric optical lattices. *Phys. Rev. Lett.* **100**, 103904 (2008).
25. Petermann, K. Calculated spontaneous emission factor for double-heterostructure injection lasers with gain-induced waveguiding. *IEEE J. Quantum Electron.* **15**, 566 (1979).

26. Vuckovic, J., Loncar, M., Mabuchi, H. & Scherer, A. Optimization of the Q factor in photonic crystal microcavities. *IEEE J. Quantum Electron.* **38**, 850 (2002).

27. Chalcraft, A. R. A. et al. Mode structure of coupled L3 photonic crystal cavities. *Opt. Express* **19**, 5670 (2011).

28. Xiong, W. et al. Complete polarization control in multimode fibers with polarization and mode coupling. *Light Sci. Appl.* **7**, 54 (2018).

29. Wang, H. et al. Towards optimal single-photon sources from polarized microcavities. *Nat. Photonics* **13**, 770 (2019).

30. He, H. et al. Polarized three-photon-pumped laser in a single MOF microcrystal. *Nat. Commun.* **7**, 11087 (2016).

31. Weissflog, M. A. et al. Far-field polarization engineering from nonlinear nanoresonators. *Laser Photonics Rev.* **16**, 2200183 (2022).

32. Wang, F. et al. Fundamentals and applications of topological polarization singularities. *Front. Phys.* **10**, 198 (2022).

33. Forbes, A., de Oliveira, M. & Dennis, M. R. Structured light. *Nat. Photonics* **15**, 253 (2021).

34. Feng, L., Wong, Z. J., Ma, R.-M., Wang, Y. & Zhang, X. Single-mode laser by parity-time symmetry breaking. *Science* **346**, 972 (2014).

35. Kim, M., Kwon, K., Shim, J., Jung, Y. & Yu, K. Partially directional microdisk laser with two Rayleigh scatterers. *Opt. Lett.* **39**, 2423 (2014).

36. Wiersig, J. Sensors operating at exceptional points: General theory. *Phys. Rev. A* **93**, 033809 (2016).

37. Yang, J. et al. Enhanced emission from a single quantum dot in a microdisk at a deterministic diabolical point. *Opt. Express* **29**, 14231 (2021).

38. Zhu, J. et al. Local chirality at exceptional points in optical whispering-gallery microcavities. *Phys. Rev. A* **108**, L041501 (2023).

39. Fong, C. F., Ota, Y., Arakawa, Y., Iwamoto, S. & Kato, Y. K. Chiral modes near exceptional points in symmetry broken H1 photonic crystal cavities. *Phys. Rev. Res.* **3**, 043096 (2021).

40. Khanbekyan, M. & Wiersig, J. Decay suppression of spontaneous emission of a single emitter in a high-Q cavity at exceptional points. *Phys. Rev. Res.* **2**, 023375 (2020).

41. Pick, A. et al. General theory of spontaneous emission near exceptional points. *Opt. Express* **25**, 12325 (2017).

42. Lin, Z., Pick, A., Lončar, M. & Rodriguez, A. W. Enhanced spontaneous emission at third-order dirac exceptional points in inverse-designed photonic crystals. *Phys. Rev. Lett.* **117**, 107402 (2016).

43. Silberstein, N., Behrends, J., Goldstein, M. & Ilan, R. Berry connection induced anomalous wave-packet dynamics in non-hermitian systems. *Phys. Rev. B* **102**, 245147 (2020).

44. Bergholtz, E. J., Budich, J. C. & Kunst, F. K. Exceptional topology of non-hermitian systems. *Rev. Mod. Phys.* **93**, 015005 (2021).

45. Lalanne, P., Yan, W., Vynck, K., Sauvan, C. & Hugonin, J.-P. Light interaction with photonic and plasmonic resonances. *Laser Photonics Rev.* **12**, 1700113 (2018).

46. Gigli, C. et al. Quasinormal-mode non-hermitian modeling and design in nonlinear nano-optics. *ACS Photonics* **7**, 1197 (2020).

47. Lalanne, P. et al. Quasinormal mode solvers for resonators with dispersive materials. *J. Opt. Soc. Am. A* **36**, 686 (2019).

48. Srinivasan, K., Borselli, M., Painter, O., Stintz, A. & Krishna, S. Cavity q, mode volume, and lasing threshold in small diameter algaas microdisks with embedded quantum dots. *Opt. Express* **14**, 1094 (2006).

49. Silva, A. G. et al. Quantum dot dipole orientation and excitation efficiency of micropillar modes. *Opt. Express* **16**, 19201 (2008).

50. Usman, M., Ryu, H., Woo, I., Ebert, D. S. & Klimeck, G. Moving toward nano-tcad through multimillion-atom quantum-dot simulations matching experimental data. *IEEE Trans. Nanotechnol.* **8**, 330 (2009).

51. Cortez, S., Krebs, O., Voisin, P. & Gérard, J. M. Polarization of the interband optical dipole in InAs/GaAs self-organized quantum dots. *Phys. Rev. B* **63**, 233306 (2001).

52. Qian, C. et al. Enhanced strong interaction between nanocavities and *p*-shell excitons beyond the dipole approximation. *Phys. Rev. Lett.* **122**, 087401 (2019).

53. Li, B.-B. et al. Single nanoparticle detection using split-mode microcavity Raman lasers. *Proc. Natl Acad. Sci. USA* **111**, 14657 (2014).

54. Yang, J. et al. Diabolical points in coupled active cavities with quantum emitters. *Light Sci. Appl.* **9**, 6 (2020).

55. Kippenberg, T. J., Spillane, S. M. & Vahala, K. J. Modal coupling in traveling-wave resonators. *Opt. Lett.* **27**, 1669 (2002).

56. Li, Q., Eftekhar, A. A., Xia, Z. & Adibi, A. Azimuthal-order variations of surface-roughness-induced mode splitting and scattering loss in high-Q microdisk resonators. *Opt. Lett.* **37**, 1586 (2012).

57. Moiseyev, N. & Friedland, S. Association of resonance states with the incomplete spectrum of finite complex-scaled hamiltonian matrices. *Phys. Rev. A* **22**, 618 (1980).

58. Zhu, J. et al. Intuitive model of exceptional points in an optical whispering-gallery microcavity perturbed by nanoparticles. *Phys. Rev. A* **101**, 053842 (2020).

59. Yuan, L., Lin, Q., Xiao, M. & Fan, S. Synthetic dimension in photonics. *Optica* **5**, 1396 (2018).

60. Zhou, X.-F. et al. Dynamically manipulating topological physics and edge modes in a single degenerate optical cavity. *Phys. Rev. Lett.* **118**, 083603 (2017).

61. Yuan, L. et al. Photonic gauge potential in one cavity with synthetic frequency and orbital angular momentum dimensions. *Phys. Rev. Lett.* **122**, 083903 (2019).

62. Dutt, A. et al. A single photonic cavity with two independent physical synthetic dimensions. *Science* **367**, 59 (2020).

63. Liu, W. et al. Circularly polarized states spawning from bound states in the continuum. *Phys. Rev. Lett.* **123**, 116104 (2019).

Acknowledgements

Author contributions

X.X., Q.G., K.J. supervised the research project. J.Y. designed and fabricated the devices and conducted the optical measurements. S.S., S.Y., R.Z., B.F. and X.C. helped perform the experiments., X.X., X.Z., Y.Q., Z.Z. conducted the theoretical discussion and data analysis. J.Y. and H.L. conducted and discussed the numerical simulation for far-field polarization. All the authors have contributed to writing the manuscript.

Competing interests

The authors declare no competing interests.

Additional information

Supplementary information The online version contains supplementary material available at https://doi.org/10.1038/s42005-023-01508-2.

Correspondence and requests for materials should be addressed to Xiulai Xu.

Peer review information *Communications Physics* thanks Nan Zhang and the other, anonymous, reviewer(s) for their contribution to the peer review of this work. A peer review file is available.

Reprints and permission information is available at http://www.nature.com/reprints

Publisher's note Springer Nature remains neutral with regard to jurisdictional claims in published maps and institutional affiliations.